



## Article

# Photothermal Regulated Nanozyme of CuFeS<sub>2</sub> Nanoparticles for Efficiently Promoting Wound Healing Infected by Multidrug Resistant Bacteria

Zezhong Liu †, Zengxu Liu †, Zhen Zhao, Danxia Li, Pengfei Zhang, Yanfang Zhang, Xiangyong Liu, Xiaoteng Ding \* and Yuanhong Xu

Institute of Biomedical Engineering, College of Life Sciences, Qingdao University, 308 Ningxia Road, Qingdao 266071, China; lzz56066@163.com (Z.L.); zengxu1996l@163.com (Z.L.); zhaozhenciac@163.com (Z.Z.); ldxy2018@163.com (D.L.); pfzhang0106@163.com (P.Z.); zyf183162@163.com (Y.Z.); z337047@163.com (X.L.); yhxu@qdu.edu.cn (Y.X.)

\* Correspondence: xtding@qdu.edu.cn

† These authors contributed equally to this work.

**Abstract:** Peroxidase-mediated chemokinetic therapy (CDT) can effectively resist bacteria; however, factors such as the high dosage of drugs seriously limit the antibacterial effect. Herein, CuFeS<sub>2</sub> nanoparticles (NPs) nanozyme antibacterial system with the photothermal effect and peroxidase-like catalytic activity are proposed as a combined antibacterial agent with biosafety, high-efficiency, and broad-spectrum antibacterial ability. In addition, the as-obtained CuFeS<sub>2</sub> NPs with a low doses of Cu<sup>+</sup> and Fe<sup>3+</sup> can change the permeability of bacterial cell membranes and break the antioxidant balance by consuming intracellular glutathione (GSH), which results in more conducive ROS production. Meanwhile, the photothermal heating can regulate the CuFeS<sub>2</sub> NPs close to their optimal reaction temperature (60 °C) to release more hydroxyl radical in low concentrations of H<sub>2</sub>O<sub>2</sub> (100 μM). The proposed CuFeS<sub>2</sub> NPs-based antibacterial system achieve more than 99% inactivation efficiency of methicillin-resistant Staphylococcus aureus (10<sup>6</sup> CFU mL<sup>-1</sup> MRSA), hyperspectral bacteria β-Escherichia coli (10<sup>6</sup> CFU mL<sup>-1</sup> ESBL) and Pseudomonas aeruginosa (10<sup>6</sup> CFU mL<sup>-1</sup> PA), even at low concentration (2 μg mL<sup>-1</sup>), which is superior to those of the conventional CuO NPs at 4 mg mL<sup>-1</sup> reported in the literature. In vivo experiments further confirm that CuFeS<sub>2</sub> NPs can effectively treat wounds infected by MRSA and promote the wound healing. This study demonstrates that excellent antibacterial ability and good biocompatibility make CuFeS<sub>2</sub> NPs a potential anti-infection nanozyme with broad application prospects.



**Citation:** Liu, Z.; Liu, Z.; Zhao, Z.; Li, D.; Zhang, P.; Zhang, Y.; Liu, X.; Ding, X.; Xu, Y. Photothermal Regulated Nanozyme of CuFeS<sub>2</sub> Nanoparticles for Efficiently Promoting Wound Healing Infected by Multidrug Resistant Bacteria. *Nanomaterials* **2022**, *12*, 2469. <https://doi.org/10.3390/nano12142469>

Academic Editor: Witold Łojkowski

Received: 10 June 2022

Accepted: 8 July 2022

Published: 19 July 2022

**Publisher's Note:** MDPI stays neutral with regard to jurisdictional claims in published maps and institutional affiliations.



**Copyright:** © 2022 by the authors. Licensee MDPI, Basel, Switzerland. This article is an open access article distributed under the terms and conditions of the Creative Commons Attribution (CC BY) license (<https://creativecommons.org/licenses/by/4.0/>).

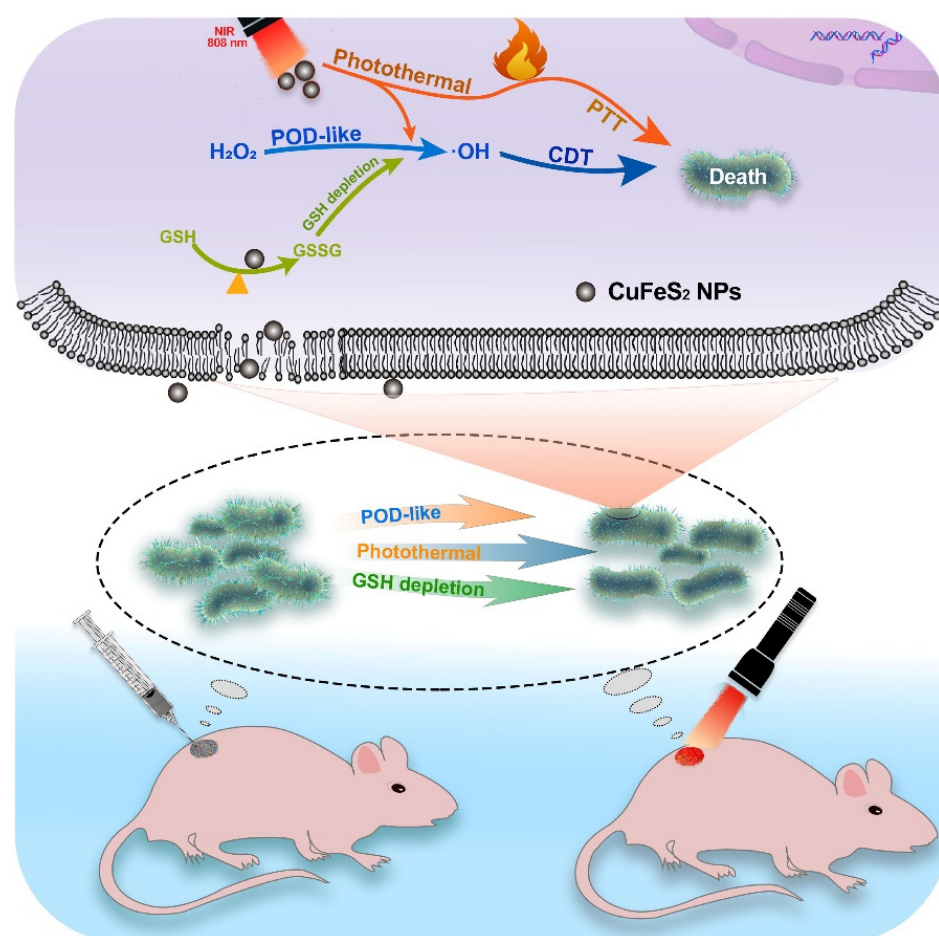
**Keywords:** bacterial infection; CuFeS<sub>2</sub> NPs; peroxidase; photothermal effect; combined antibacterial

## 1. Introduction

With the continuous development of drug-resistant strains, bacterial infectious diseases are a major threat to global health [1–3]. In traditional treatment strategy, antibiotics are the most effective and conventional method for the treatment of bacterial infection. However, the heavy use of antibiotics has led to the occurrence of multiple drug resistance bacteria, which causes a sharp decline in the efficacy of antibiotics [4]. Consequently, effective antimicrobial agents are severely needed, as a substitute to antibiotics. The development of new antibacterial platforms based on nanomaterials, Ag- or Cu-based, have been well-developed and regarded as efficiently antibacterial, but high-dose applications still suffered from potentially non-negligible biological toxicity, due to their intrinsic properties of heavy metals. Owing to the advantages of high catalytic activity, substrate selectivity, higher stability, and adaptability to special environments [5], nanozymes have been diffusely applied in the areas of antibacterial treatment, in order to treat the infected wounds

in animals [6–8]. For example, peroxidase mimics can specifically facilitate the conversion of hydrogen peroxide ( $\text{H}_2\text{O}_2$ ) to the more oxidizing hydroxyl radical ( $\bullet\text{OH}$ ), in order to achieve a better antibacterial effect, thus effectively avoiding the side effects of high concentration of  $\text{H}_2\text{O}_2$  to animal healthy tissues [9,10]. Some inorganic nanomaterials with peroxidase-like activity have been reported, such as  $\text{V}_2\text{O}_5$  QDs, Au NPs, and  $\text{MoS}_2$  nanomaterials, etc. [3,11]. Although these nanomaterials have shown great potential for antimicrobial use in peroxidase-mediated chemokinetic therapy (CDT), their antibacterial effects are limited, due to the insufficient production of hydroxyl radicals ( $\bullet\text{OH}$ ) and short effective action distance of hydroxyl radicals [12]. Photothermal therapy (PTT), which can use local near-infrared (NIR) light to cause high temperatures or improve the catalytic activity of nanozymes, which has been diffusely used in mice tumor treatment and antibacterial because of their advantages, i.e., less invasiveness, fewer side effects, and better controllability, compared with other antibacterial drugs. However, long time exposure to high power density NIR may induce skin destruction and bacterial heat resistance [13]. Since the antibacterial therapy alone is not efficient enough to reach satisfying efficiency, a combined therapy strategy is expected to compensate for each other, in order to overcome the shortcomings of single-mode therapy, thus greatly improving the antibacterial effect [14]. While enhancing the antibacterial efficiency of CDT, by means of multi-mode combination and ROS release, the antioxidant system of bacterial cells should not be ignored [15]. Glutathione (GSH) is an intracellular reducing substance that consumes hydroxyl radicals to inhibit the therapeutic effect of CDT. Therefore, the consumption of GSH helps to further improve the therapeutic effect of CDT [16,17]. In order to treat bacterial-infected wounds and promote wound healing, it is necessary to develop efficient and safe nano antibacterial materials. In addition, the efficient nanozyme against pathogenic bacteria with the synergistic effect of CDT, PTT, and GSH consumption capacity has rarely been reported.

Herein, we prepared and characterized the  $\text{CuFeS}_2$  nanoparticles (NPs) and evaluated the antibacterial efficacy against both Gram-positive and -negative bacteria. Under the irradiation of a NIR laser, the activity of  $\text{CuFeS}_2$  NPs peroxidase is effectively enhanced, under the condition that  $\text{CuFeS}_2$  does not produce temperatures that are too high, and more hydroxyl radicals are released, so as to kill pathogenic bacteria more effectively. In addition, under simulated physiological conditions,  $\text{CuFeS}_2$  NPs showed the ability to consume GSH. Based on the above advantages, the as-obtained  $\text{CuFeS}_2$  NPs can consume the GSH in bacteria and effectively fight pathogenic bacteria via the combination of PTT and ROS-mediated CDT (Scheme 1). High-resolution transmission electron microscope (HRTEM) and transmission electron microscope (TEM) were used to characterize the morphology. The UV–VIS absorption spectrum and fluorescence methods were used to detect the hydroxyl radical and characterize the enzyme activity of  $\text{CuFeS}_2$  NPs.



**Scheme 1.** Scheme of the treatment of bacterial wound infection in mice.

## 2. Materials and Methods

### 2.1. Synthesis of CuFeS<sub>2</sub> Nanoparticles

With deionized water as the solvent, 50 mL of deionized water was taken into a conical flask. The water bath was heated to 90 °C for more than 5 min, in order to effectively eliminate dissolved oxygen. Next, FeSO<sub>4</sub>·7H<sub>2</sub>O (5.6 mg) and CuCl<sub>2</sub>·2H<sub>2</sub>O (17.0 mg) were dispersed into the deionized water (1.2 mL), adjusting the pH of the mixed solution to about 12.0. Then, Na<sub>2</sub>S·9H<sub>2</sub>O (97.0 mg) was quickly added into the above mixed solution directly, and the solution turned black. Finally, the samples were converged by centrifugation, washed three times with deionized water, and freeze-dried for use.

### 2.2. POD-like Activity and Kinetic Assay

In order to explore the peroxidase-mimic activity of CuFeS<sub>2</sub> NPs, TMB was selected as the chromogenic substrate, and the UV absorption changes (652 nm) of the reaction system were observed and recorded in the presence of H<sub>2</sub>O<sub>2</sub> in the acetate buffer (0.1 M, pH 4.0). Accordingly, 0.1 mL CuFeS<sub>2</sub> NPs suspension (40 µg mL<sup>-1</sup>), 0.025 mL H<sub>2</sub>O<sub>2</sub> (0.5 mM), and 0.025 mL TMB (0.5 mM) were added to 0.85 mL acetate buffer. A total of four groups of reaction systems were set: TMB + H<sub>2</sub>O<sub>2</sub>, CuFeS<sub>2</sub> + TMB, CuFeS<sub>2</sub> + H<sub>2</sub>O<sub>2</sub>, and TMB + CuFeS<sub>2</sub> + H<sub>2</sub>O<sub>2</sub> at room temperature for 5 min. Then, the color pictures of each reaction system were taken, and the UV spectra of different systems were scanned by ultraviolet spectrophotometer. The temperature (22~90 °C) and pH (2.0~11.0) tolerance of the peroxidase of CuFeS<sub>2</sub> NPs were studied with an acetate buffer (pH 4.0, 0.1 M) as the background, and the maximum absorbance of each group was defined as 100%. The peroxidase kinetics of CuFeS<sub>2</sub> NPs was studied by absorbance monitoring at 652 nm under different conditions. In the pH 4.0 acetate buffer, the concentration of CuFeS<sub>2</sub>

NPs in the reaction system was  $40 \mu\text{g mL}^{-1}$ , and the concentration of  $\text{H}_2\text{O}_2$  or TMB of one substrate was fixed, respectively, while the concentration of the other substrate was changed. The total system was 1 mL, and the reaction time was 10 min. After 10 min of reaction, the absorbance of each system was measured. The kinetic parameters of  $\text{CuFeS}_2$  NPs peroxidase were calculated according to the Michaelis equation:

$$\frac{1}{V} = \frac{K_m}{V_{\max}} \times \frac{1}{[S]} + \frac{1}{V_{\max}} \quad (1)$$

where  $K_m$  delegates the Mie constant,  $[S]$  delegates the substrate concentration, and  $V_{\max}$  stands for the maximum reaction rate. The reaction rate and substrate concentration were fitted by the Michaelis–Menten equation,  $V_{\max}$  and the kinetic parameters  $K_m$  were obtained by Lineweave–Burk plot.

### 2.3. Detection of Hydroxyl Radical

The hydroxyl radical was detected by fluorescence method. In order to detect  $\bullet\text{OH}$  in the reaction catalyzed by  $\text{CuFeS}_2$  NPs peroxidase, TA was selected as a fluorescent probe. TA itself had no fluorescence. When TA captured  $\bullet\text{OH}$ , it formed 2-hydroxyl terephthalic acid (TAOH) with a strong fluorescence emission peak at 435 nm. In phosphate buffer solution (pH 7.4, 0.1 M), the concentration of each component in the reaction system was  $\text{CuFeS}_2$  NPs ( $40 \mu\text{g mL}^{-1}$ ), Ta (0.5 mM), and  $\text{H}_2\text{O}_2$  (1.0 mM). Four groups of reaction systems were set: Ta, Ta +  $\text{H}_2\text{O}_2$ , Ta +  $\text{CuFeS}_2$ , and Ta +  $\text{H}_2\text{O}_2$  +  $\text{CuFeS}_2$ . The samples were placed at room temperature for 12 h, and the fluorescence spectra of each sample were measured by a fluorometer (Edinburgh FS5).

Electron spin resonance spectroscopy (ESR) measurements were made at room temperature on a standard X-band Bruker E-500 EPR spectrometer (Germany). DMPO (5, 5-dimethyl-1-pyrrolin-N-oxide) was used as a trap to capture free  $\bullet\text{OH}$  to form DMPO/ $\bullet\text{OH}$  spin adducts. The concentrations of each component in the system were  $\text{H}_2\text{O}_2$  (10 mM),  $\text{CuFeS}_2$  ( $40 \mu\text{g mL}^{-1}$ ), and DMPO (40 mM). Four groups of samples were set to be tested: DMPO, DMPO +  $\text{H}_2\text{O}_2$ , DMPO +  $\text{CuFeS}_2$ , and DMPO +  $\text{H}_2\text{O}_2$  +  $\text{CuFeS}_2$ . The prepared sample solution was transferred into a quartz capillary tube and placed for 30 min to monitor the ESR signal. All of the above operations were performed in a NAAC buffer (0.1 M, pH 4.0). All ESR spectra were obtained with 1 G field modulation, 100 G scanning range, and 20 mW microwave power.

### 2.4. Bacterial Culture and In Vitro Bacteriostatic Experiment

Bacterial culture and in vitro bacteriostatic experiment. *Pseudomonas aeruginosa* (PA), hyperspectral  $\beta$ -lactamase-producing *Escherichia coli* (ESBL), and methicillin-resistant *Staphylococcus aureus* (MRSA) were inoculated in LB liquid medium ( $37^\circ\text{C}$ , 180 rpm) for 12 h, respectively. The obtained bacterial solution was diluted to  $10^6$  CFU  $\text{mL}^{-1}$ , and the following treatments were performed: PBS,  $\text{H}_2\text{O}_2$ ,  $\text{CuFeS}_2$ ,  $\text{CuFeS}_2$  +  $\text{H}_2\text{O}_2$ , PBS + NIR,  $\text{H}_2\text{O}_2$  + NIR,  $\text{CuFeS}_2$  + NIR, and  $\text{CuFeS}_2$  +  $\text{H}_2\text{O}_2$  + NIR, which were treated with NIR ( $1 \text{ W cm}^{-2}$ , 808 nm) for 5 min. The total system of each experimental group was 300  $\mu\text{L}$ , including  $10^6$  CFU  $\text{mL}^{-1}$  bacterial suspension,  $2 \mu\text{g mL}^{-1}$   $\text{CuFeS}_2$  NPs, and 0.1 mM  $\text{H}_2\text{O}_2$ . After incubation at  $37^\circ\text{C}$  for 30 min, 100  $\mu\text{L}$  of the treated bacterial solution was taken and evenly coated on the plate. The bacteria were incubated overnight at  $37^\circ\text{C}$ , observed, and photographed.

### 2.5. Fluorescence Detection of Living/Dead Bacteria

In order to visually identify the live/dead state of the bacteria, the bacterial samples treated with different methods were fluorescently stained. The concentration of bacterial liquid was  $10^8$  CFU  $\text{mL}^{-1}$ , and 8 groups of experiments were set for the following treatments: PBS,  $\text{H}_2\text{O}_2$ ,  $\text{CuFeS}_2$ ,  $\text{CuFeS}_2$  +  $\text{H}_2\text{O}_2$ , PBS + NIR,  $\text{H}_2\text{O}_2$  + NIR,  $\text{CuFeS}_2$  + NIR,  $\text{CuFeS}_2$  +  $\text{H}_2\text{O}_2$  + NIR, NIR refers to under the irradiation of 808 nm NIR light ( $808 \text{ nm}$ ,  $1 \text{ W cm}^{-2}$ ) for 5 min and incubated with bacteria at  $37^\circ\text{C}$  for 30 min. Then, the unbounded

dye was washed using PBS after being incubated at 37 °C for 15 min using SYTO9 and PI fluorescent dye. Drop-coated glass slides were used for sample preparation. Bacteria were observed under a positive fluorescence microscope, and fluorescence staining images were taken. Bacteria in normal state showed green fluorescence, while bacteria in dead state showed red fluorescence.

#### 2.6. Bacterial ROS Fluorescence Detection

DCFH-DA (10 µM) was added into 20 mL 0.9% NaCl solution and co-incubated with  $10^8$  CFU/mL bacteria for 30 min. The combined DCFH-DA was removed by centrifugation at 8000 RPM for 5 min. The bacterial cells were treated in different ways, as follows: PBS, H<sub>2</sub>O<sub>2</sub>, CuFeS<sub>2</sub>, CuFeS<sub>2</sub> + H<sub>2</sub>O<sub>2</sub>, PBS + NIR, H<sub>2</sub>O<sub>2</sub> + NIR, CuFeS<sub>2</sub> + NIR, and CuFeS<sub>2</sub> + H<sub>2</sub>O<sub>2</sub> + NIR were treated with Nir (808 nm, 1 W cm<sup>-2</sup>) for 5 min and incubated at 37 °C for 4 h. Fluorescence intensity was measured with a fluorometer and observed and photographed under a fluorescence microscope.

#### 2.7. SEM Characterization of Bacteria

Methicillin-resistant *Staphylococcus aureus* (MRSA), hyperspectral β-lactamase-producing *Escherichia coli* (ESBL), and *Pseudomonas aeruginosa* (PA) were treated as follows: after incubation with CuFeS<sub>2</sub> + H<sub>2</sub>O<sub>2</sub> at 37 °C for 4 h, each reaction system was centrifuged at 3000 RPM for 5 min, and then washed with PBS for 3 times. Then, they were fixed with 2.5% glutaraldehyde, overnight at 4 °C, followed by dehydration with ethanol solution of different concentrations, followed by treatment with 50% and 100% isoamyl acetate, the final zero-point drying, smear sample preparation.

#### 2.8. Biocompatibility Evaluation of CuFeS<sub>2</sub> Nanomaterials

The biological toxicity of CuFeS<sub>2</sub> nanomaterials was evaluated by hemolysis test. The specific procedures were as follows. Fresh blood of rats was taken, centrifuged (15 min, 1500 rpm) to concentrate red blood cells, and washed with normal saline for 3 times. The red blood cell suspension was diluted to 5%, treated with normal saline, water, and different concentrations of CuFeS<sub>2</sub> NPs (25, 50, and 100 µg mL<sup>-1</sup>), incubated for 3 h at 37 °C, and centrifuged (5 min, 11,000 rpm). The absorbance value of the supernatant at 540 nm was determined. The hemolysis rate of CuFeS<sub>2</sub> NPs was computed with water and normal saline treatment groups as controls.

MTT assay was carried out to assess the cytotoxicity of CuFeS<sub>2</sub> NPs using L929 fibroblasts. The procedure was as follows. Approximately 5000 cells were inoculated in each well in a 96-well plate medium containing 10% FBS and 1% penicillin-streptomycin. The CO<sub>2</sub> cell incubator was cultured until the cells were filled, and different concentrations of CuFeS<sub>2</sub> NPs samples were added to continue the culture. After incubation for 24 h, 20 µL 5 mg mL<sup>-1</sup> MTT were added to each well and continued to incubate for 4 h. Then, the obtained purple formazan was dissolved by DMSO (150 µL per well) with gentle shaking for 10 min. The absorbance at 490 nm was determined, and the cell viability was calculated.

In order to evaluate the compatibility of CuFeS<sub>2</sub> in vivo, samples with concentrations of 40 and 80 µg mL<sup>-1</sup> were prepared and injected into rats by intraperitoneal injection. The control group was given with the same volume of PBS buffer. After one-week treatment, the treated rats were killed, and the liver, heart, spleen, kidney, lung, and other organs were removed and fixed with formaldehyde; paraffin sections were made for histological analysis. At the same time, serum samples were collected to determine physiological indexes.

#### 2.9. The Rats Wound Model

The Sprague–Dawley (SD) rats were aged 6 weeks, with a mean weight of 180 g. All the rats were randomly distributed into eight groups (each group of three) and slashed with about 0.6 cm wound area on their backs. After that, the wound area of the rats was injected with  $1 \times 10^6$  of *S. aureus*, which was then treated with different antibacterial groups of PBS,

H<sub>2</sub>O<sub>2</sub>, CuFeS<sub>2</sub>, CuFeS<sub>2</sub> + H<sub>2</sub>O<sub>2</sub>, PBS + NIR, H<sub>2</sub>O<sub>2</sub> + NIR, CuFeS<sub>2</sub> + NIR, and CuFeS<sub>2</sub> + H<sub>2</sub>O<sub>2</sub> + NIR. To harvest the wound tissue, the mice were sacrificed on the seventh day of the experiment, and the skin was excised, including the entire wound with adjacent normal skin. For histological examination, the wound tissues were gathered after the seventh day of the experiment and fixed in 4% paraformaldehyde solution. Then, the tissue samples were embedded in paraffin and stained with hematoxylin and eosin (H&E).

### 3. Results and Discussion

#### 3.1. Preparation and Characterization of CuFeS<sub>2</sub> NPs

The antibacterial nanomaterials were synthesized using CuCl<sub>2</sub>·2H<sub>2</sub>O, FeSO<sub>4</sub>·7H<sub>2</sub>O, and Na<sub>2</sub>S·9H<sub>2</sub>O as the precursors [18]. The morphology of the as-prepared CuFeS<sub>2</sub> NPs was characterized by TEM (Figure 1a) and HRTEM (Figure 1b). It can be seen that the as-obtained nanoparticles have uniform size, and the particle size is calculated to be  $10.38 \pm 1.39$  nm (Figures S1 and S10), as computed to counting the CuFeS<sub>2</sub> particles of the TEM images. Meanwhile, the HRTEM image shows that CuFeS<sub>2</sub> NPs have a parallel and ordered crystal lattice with 0.305 nm lattice spacing, corresponding to the (111) crystal of CuFeS<sub>2</sub> (JCPDS 41-1404), which fits in with the literature reports [18]. In order to demonstrate the crystal characteristics of the product, XRD was performed, and the diffraction peaks were basically consistent with the standard card of the CuFeS<sub>2</sub> crystal and in good agreement with the HRTEM data results (Figure 1c). The above results preliminarily prove that the CuFeS<sub>2</sub> NPs were successfully synthesized. In order to study the element composition and valence of CuFeS<sub>2</sub> NPs, XPS analysis was performed. According to the XPS spectra (Figure 1d), the samples were composed of Cu, Fe, and S elements, and their corresponding signal peaks were located at 931.81 eV, 710.70 eV, and 161.90 eV, respectively [19]. The high-resolution XPS spectra of Fe, S, and Cu for CuFeS<sub>2</sub> NPs were analysed, respectively. Figure 1e shows the high-resolution spectrogram of Cu 2p; the peaks of 2p<sup>1/2</sup> and Cu 2p<sup>3/2</sup> at 952.70 eV and 932.90 eV were obtained by peak separation fitting, which are attributed to Cu(I) in CuFeS<sub>2</sub> [20]. Anyway, there was no signal peak at 942 eV, reflecting that there was almost no Cu(II) in the prepared CuFeS<sub>2</sub>, which is consistent with the previously reported results that only monovalent copper atoms exist in chalcopyrite structures [21]. Figure 1f is the high-resolution XPS spectrum of Fe 2p, the peaks at 724.83 eV and 711.15 eV are attributed to Fe<sup>3+</sup><sub>2p</sub><sup>1/2</sup> and Fe<sup>3+</sup><sub>2p</sub><sup>3/2</sup>, while the double peaks at 713.49 eV and 719.49 eV are attributed to Fe(II) [22–24]. Figure 1g shows the high-resolution spectrum of S 2p, and the peak at 162.18 eV is attributed to the presence of S<sup>2-</sup>. The peak at 163.97 eV belongs to the polysulfide (S<sub>n</sub><sup>2-</sup>) formed by sulphur vacancy on the surface of CuFeS<sub>2</sub>. The peaks at 168.66 eV and 169.74 eV are attributed to the presence of sulfate, possibly due to the oxidation of on the CuFeS<sub>2</sub> surfaces [25,26]. The XPS characterization further confirmed that CuFeS<sub>2</sub> was successfully synthesized, which is consistent with the XRD and HRTEM results. The photothermal conversion ability of the CuFeS<sub>2</sub> NPs was studied by irradiating CuFeS<sub>2</sub> NPs aqueous solution with an 808 nm NIR laser at 1.0 W cm<sup>-2</sup>. Figure 1h shows that the CuFeS<sub>2</sub> NPs have effective photo thermal heating, and the corresponding solution temperature increased with the concentration of CuFeS<sub>2</sub> NPs. In the presence of CuFeS<sub>2</sub> NPs (1000 µg mL<sup>-1</sup>) and under 60 s NIR laser irradiation, the dispersion temperature increased to 50 °C (close to their optimum enzymatic temperature), demonstrating that CuFeS<sub>2</sub> NPs have excellent photothermal conversion ability. In Figure S2, the CuFeS<sub>2</sub> NPs still maintain good photothermal conversion ability after five heating/cooling processes under NIR laser irradiation, which proves the excellent photothermal stability of CuFeS<sub>2</sub> NPs. According to Figure S2A,B, the photothermal conversion efficiency [27] is further computed to be 29.8%, which is higher than that of traditional Au NPs (22.1%) [28]. The near infrared absorption of material with different concentrations also illustrated in Figure S8. These results proved that the prepared CuFeS<sub>2</sub> NPs could be used as a potential PTT material.

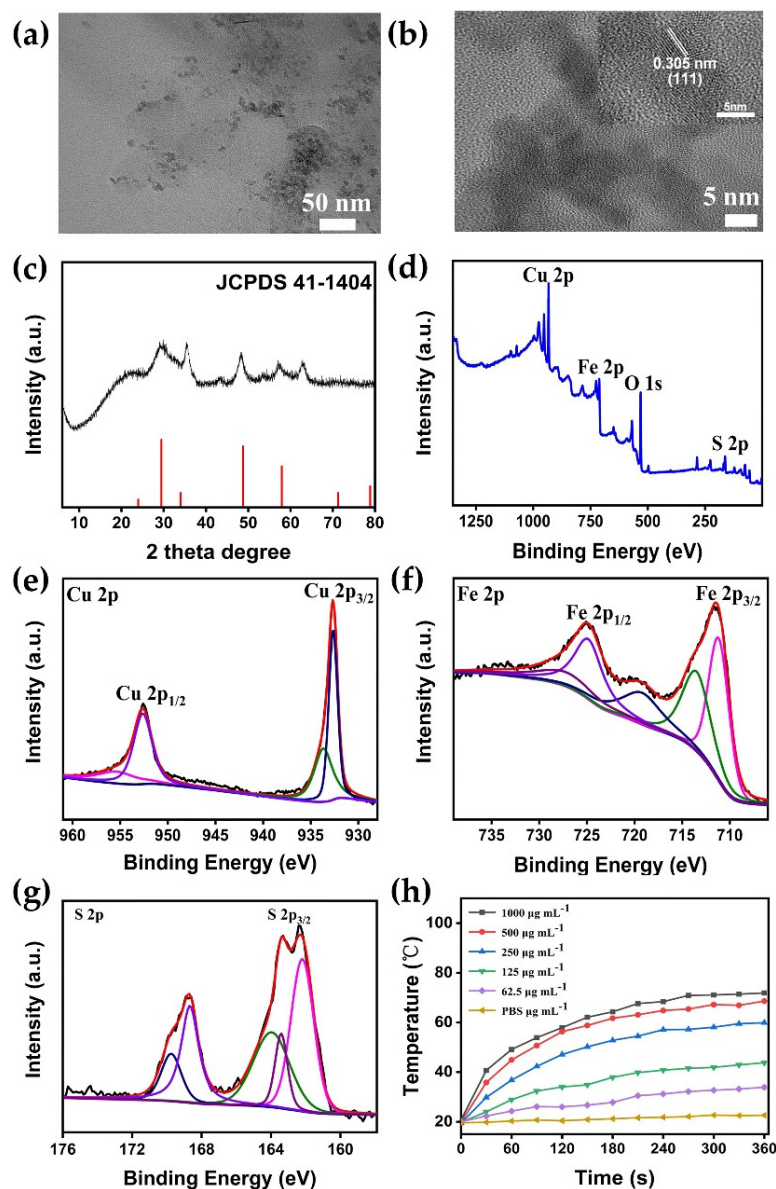


**Figure 1.** (a) TEM image, (b) HRTEM image, (c) XRD pattern, and (d) XPS survey of the prepared  $\text{CuFeS}_2$  NPs; high-resolution XPS spectra of (e) Cu 2p, (f) Fe 2p, and (g) S 2p. (h) Heating curves of  $\text{CuFeS}_2$  NPs with different concentrations (0, 62.5, 125, 250, 500, and 1000  $\mu\text{g mL}^{-1}$ ) under near-infrared light (808 nm,  $1.0 \text{ W cm}^{-2}$ ) irradiation.

### 3.2. $\text{CuFeS}_2$ NPs Peroxidase Activity and Hydroxyl Radical Production

To study the peroxidase-like catalytic properties of  $\text{CuFeS}_2$  NPs, the ultraviolet spectra were used to measure the absorbance of TMB, ABTS, and OPD as color substrates in the existence of  $\text{H}_2\text{O}_2$ . The three substrates all produced specific color changes, and their corresponding characteristic absorption peaks were also observed in Figure 2a, which preliminarily proved that  $\text{CuFeS}_2$  NPs had intrinsic peroxidase activity. The prepared material can facilitate the reaction of  $\text{H}_2\text{O}_2$  to produce hydroxyl radical, leading to the oxidation of TMB to ox-TMB, which changes the dispersion from colorless to blue. Compared with the control group, with only TMB or  $\text{H}_2\text{O}_2$ , the reaction solution could change from colorless to dark blue, producing a strong UV absorption peak at 652 nm upon the addition of both TMB and  $\text{H}_2\text{O}_2$  (Figure 2b). In addition, the absorbance of the reaction system at 652 nm increased monotonically with the concentration of  $\text{CuFeS}_2$  NPs (Figure 2f), and the UV-VIS absorption spectra of reaction systems containing different concentrations of  $\text{CuFeS}_2$  (0, 6.25, 12.5, 25.0, 50.0, and 100  $\mu\text{g mL}^{-1}$ ), indicating that the conversion of  $\text{H}_2\text{O}_2$  to hydroxyl

radical ( $\bullet\text{OH}$ ) was accelerated, which led to the acceleration of TMB oxidation. To further verify the peroxidase catalytic activity of  $\text{CuFeS}_2$  NPs, the hydroxyl radical generated in the catalytic process was monitored via the terephthalic acid (TA)-based fluorescent assays. As shown in Figure 2c and Figure S3, a fluorescence peak appears at 435 nm in the presence of  $\text{CuFeS}_2$  NPs, which reflected the generation of hydroxyl radicals. After the addition of  $\text{H}_2\text{O}_2$ , the fluorescence intensity improved much more apparently, reflecting that  $\text{CuFeS}_2$  NPs could convert  $\text{H}_2\text{O}_2$  to a hydroxyl radical. The hydroxyl radical produced in the catalysis of  $\text{CuFeS}_2$  peroxidase was further determined by ESR characterization. As can be seen from Figure 2d, four typical signal peaks, with an intensity ratio of 1:2:2:1, can be obtained when  $\text{CuFeS}_2$  and  $\text{H}_2\text{O}_2$  are present in the DMPO system, significantly different from  $\text{CuFeS}_2$  or  $\text{H}_2\text{O}_2$  alone, which proves the production of the hydroxyl radical in the system. All the results confirmed the POD-like activity of the as-obtained  $\text{CuFeS}_2$  NPs. Additionally, we verified the influence of NIR on the peroxidase catalytic activity of  $\text{CuFeS}_2$  NPs. As shown in Figure 2e and Figure S4, the absorbance of the reaction system  $\text{CuFeS}_2 + \text{H}_2\text{O}_2 + \text{TMB}$  was significantly increased under NIR illumination, and a higher fluorescence intensity was detected by the TA method, which indicates that the peroxidase-like activity of  $\text{CuFeS}_2$  NPs can be further enhanced upon the NIR light irradiation.

### 3.3. Kinetic Studies of the Enzyme-Mimic Activities of the As-Prepared $\text{CuFeS}_2$

The impacts of pH and temperature on the peroxidase-like activity of  $\text{CuFeS}_2$  NPs were explored. As shown in Figure 3a,b, the catalytic activity was good in the pH range (2.0–11.0) and a wide temperature range (22–90 °C), and the optimum pH and temperatures for  $\text{CuFeS}_2$  were 3.0 and 60 °C, respectively. It can be seen that the  $\text{CuFeS}_2$  NPs have strong temperature tolerance. Then, the steady-state kinetics analysis was carried out using TMB and  $\text{H}_2\text{O}_2$  as substrates. A typical Michaelis–Menten curve was obtained by varying the concentration of one substrate, TMB or  $\text{H}_2\text{O}_2$ , as the concentration of the other substrate was kept constant (Figure 3c,e). The linear equation (Figure 3d,f) was obtained by the double-reciprocal plotting method, Lineweaver–Burk, and the apparent kinetic parameters  $V_{\text{max}}$  and  $K_{\text{m}}$  were finally calculated and summarized in Table S1. The results show that the behavior of  $\text{CuFeS}_2$  NPs on the substrates TMB and  $\text{H}_2\text{O}_2$  followed the typical Michaelis–Menten equation. In addition, the  $\text{CuFeS}_2$  NPs have a lower  $K_{\text{m}}$  value and a higher  $V_{\text{max}}$  than natural horseradish peroxidase (HRP) and classical peroxidase analogs (Table S1) [29,30], indicating that  $\text{CuFeS}_2$  NPs have a stronger affinity for substrates TMB and  $\text{H}_2\text{O}_2$ , as well as a higher catalytic efficiency. This may be due to the large specific surface area and small size of the nanoparticles, which can expose more surface-active sites.

### 3.4. Evaluation of Antibacterial Performance of $\text{CuFeS}_2$ NPs

Because of the remarkable photothermal conversion ability and peroxidase activity of  $\text{CuFeS}_2$  NPs, MRSA, ESBL, and PA were selected as the study objects to evaluate the antibacterial performance of  $\text{CuFeS}_2$  NPs. In the absence of NIR irradiation, after treatment with  $\text{CuFeS}_2$  NPs +  $\text{H}_2\text{O}_2$ , the amount of bacterial colonies was expressively less than other groups (Figure 4). This was because of the conversion of low concentration  $\text{H}_2\text{O}_2$  into highly toxic hydroxyl radical catalyzed by  $\text{CuFeS}_2$  NPs peroxidase, which increased the killing ability of bacterial cells. However, the antimicrobial ability of this strategy is limited, and many bacteria remained. In order to improve the antibacterial efficiency, NIR illumination can achieve PTT treatment and improve the catalytic efficiency of peroxidase. It can be seen from the antibacterial experiment results that, under the NIR irradiation,  $\text{CuFeS}_2$  NPs +  $\text{H}_2\text{O}_2$  group significantly improved the antibacterial effect. It was calculated by the plate counting  $\text{CuFeS}_2$  NPs ( $2 \mu\text{g mL}^{-1}$ ) on  $1 \times 10^6$  CFU  $\text{mL}^{-1}$  MRSA, ESBL, and PA, with an antibacterial rate of more than 99%, which is superior to those of the other control groups and the conventional CuO NPs ( $4 \text{ mg mL}^{-1}$ ) reported in the literature [31]. Thus, the antimicrobial strategy, based on the combination of PPT and CDT, can effectively inhibit bacteria, while evading the use of high concentration of  $\text{H}_2\text{O}_2$  and  $\text{CuFeS}_2$  NPs and effectively avoiding the toxic and side effects. In order to evaluate the PPT/CDT

synergistic antibacterial performance of CuFeS<sub>2</sub> NPs and integrity of bacterial structure, live/dead staining assays were carried out (Figure S5). It was found that there was only a small amount of red fluorescence signals of the MRSA, ESBL, and PA cells after being treated with PBS, H<sub>2</sub>O<sub>2</sub>, CuFeS<sub>2</sub>, PBS + NIR, H<sub>2</sub>O<sub>2</sub> + NIR, or CuFeS<sub>2</sub> + NIR, indicating that the bacterial activity was normal. In contrast, the red fluorescence signals of the three bacterial cells were significantly enhanced after CuFeS<sub>2</sub> + H<sub>2</sub>O<sub>2</sub> treatment, indicating that the bacterial cell wall was seriously damaged, and the dye was bound to the nucleus. When NIR light was introduced, the red fluorescence signals of CuFeS<sub>2</sub> + H<sub>2</sub>O<sub>2</sub> + NIR-treated bacteria were enhanced, which proved that NIR light enhanced the antibacterial effects. These results were in line with the in vitro antibacterial experiments and SEM characterization, which all certified the enhanced antibacterial ability of CuFeS<sub>2</sub> NPs under NIR light.

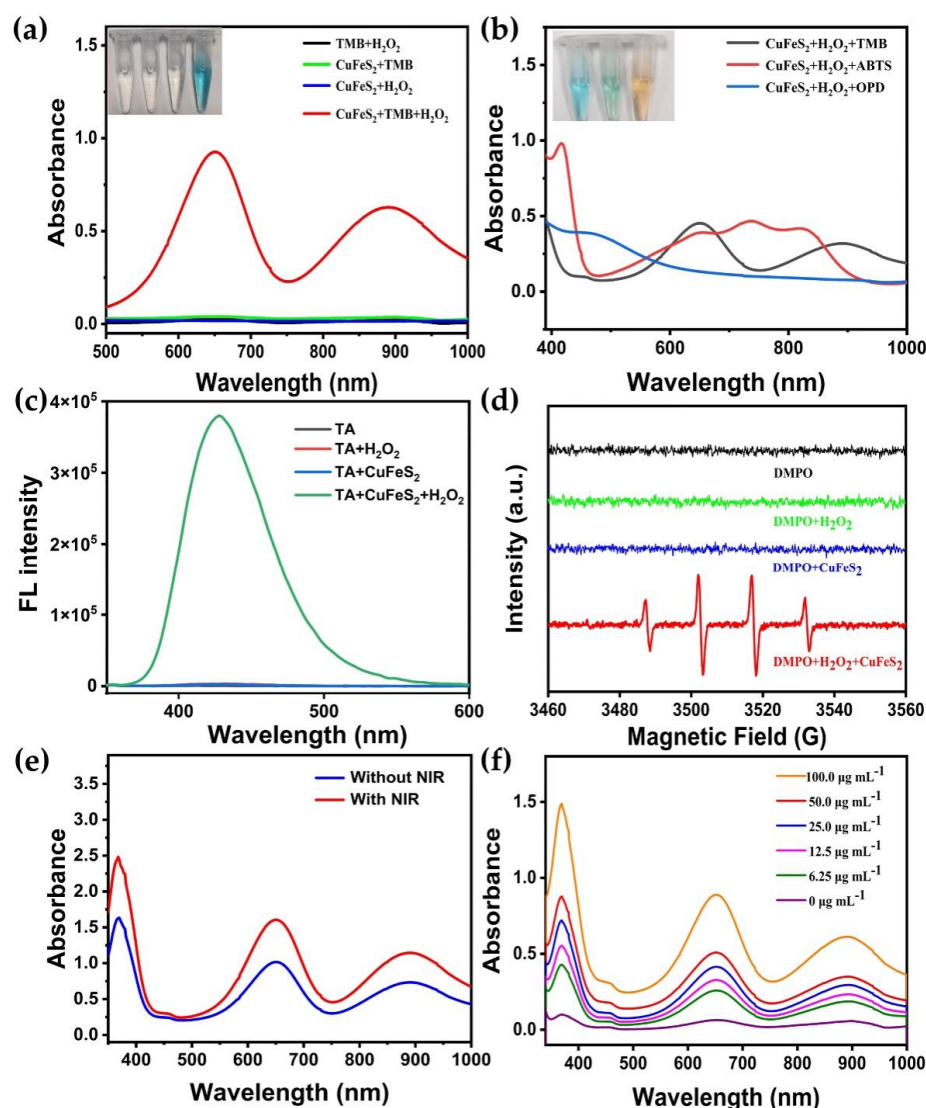


**Figure 2.** (a) The UV-VIS absorption spectra and color photos of TMB + H<sub>2</sub>O<sub>2</sub>, CuFeS<sub>2</sub> + TMB, CuFeS<sub>2</sub> + H<sub>2</sub>O<sub>2</sub>, and CuFeS<sub>2</sub> + TMB + H<sub>2</sub>O<sub>2</sub> reaction systems in NaAc HAC buffer (pH 4.0, 25 °C) after 10 min incubation. (b) The UV-VIS absorption spectra and corresponding color photos of TMB, ABTS, and OPD color systems in NaAc HAC buffer (pH 4.0, 25 °C) after incubation for 10 min. (c) The fluorescence spectra of different reaction systems: TA, TA + H<sub>2</sub>O<sub>2</sub>, TA + CuFeS<sub>2</sub>, and TA + H<sub>2</sub>O<sub>2</sub> + CuFeS<sub>2</sub>. (d) ESR. (e) The UV-VIS absorption spectra of CuFeS<sub>2</sub> peroxidase catalysis with or without NIR. (f) The UV-VIS absorption spectra of reaction systems containing different concentrations of CuFeS<sub>2</sub> (0, 6.25, 12.5, 25, 50, and 100 μg mL<sup>-1</sup>).

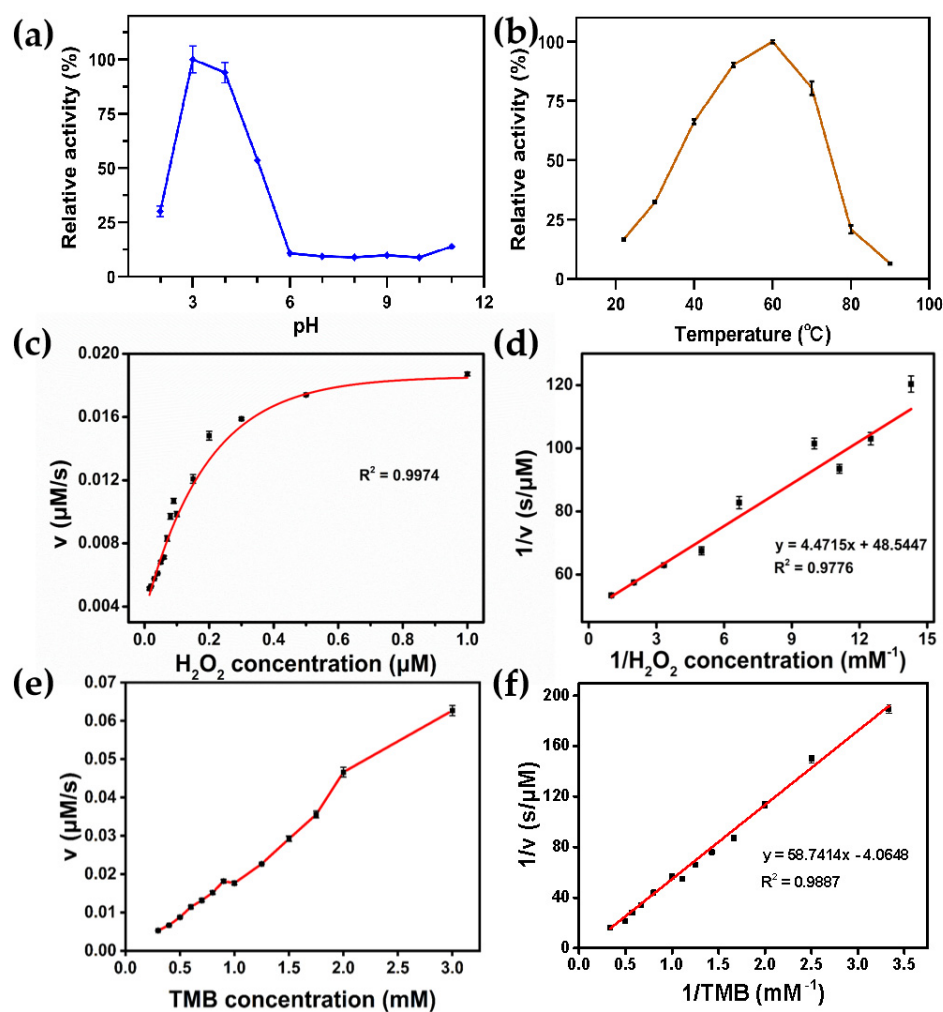


**Figure 3.** (a) The pH of CuFeS<sub>2</sub> peroxidase activity. (b) The temperature curves of CuFeS<sub>2</sub> peroxidase activity. (c–e) and (f) steady-state kinetic assay of CuFeS<sub>2</sub>.

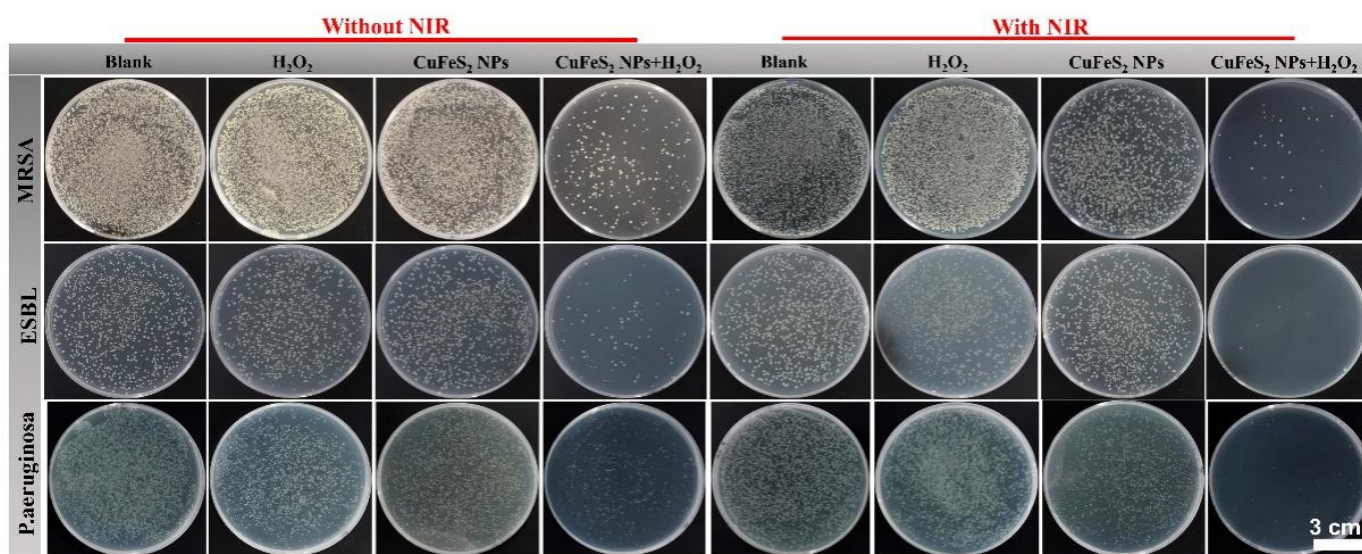


**Figure 4.** Bacterial colonies of MRSA, ESBL, and PA after different treatments of PBS, H<sub>2</sub>O<sub>2</sub>, CuFeS<sub>2</sub>, CuFeS<sub>2</sub> + H<sub>2</sub>O<sub>2</sub>, PBS + NIR, H<sub>2</sub>O<sub>2</sub> + NIR, CuFeS<sub>2</sub> + NIR, and CuFeS<sub>2</sub> + H<sub>2</sub>O<sub>2</sub> + NIR.

In order to reveal the antibacterial mechanism, DCFH-DA was used as an ROS fluorescent probe, which emitted green fluorescence after capturing ROS, for characterizing the difference of bacterial ROS in the experiment. The three strains treated by  $\text{CuFeS}_2 + \text{H}_2\text{O}_2$  showed a strong fluorescence signal, indicating that  $\text{H}_2\text{O}_2$  decomposed into a hydroxyl radical with stronger oxidation under the catalysis of  $\text{CuFeS}_2$  peroxidase (Figure 5a,b). The ROS fluorescence signals in the three strains all increased significantly, indicating that the production of hydroxyl radical was enhanced with the assistance of NIR light, which led to an increase the ROS level in the bacteria, thus achieving better bacteriostatic effect. These results were in accordance with the *in vitro* bacteriostatic experiments. To further explore the mechanism of bacterial death, the cell morphology of MRSA, ESBL-E. coli, and PA were characterized by SEM. As can be seen from Figure 5c–e, the surface of bacterial cells treated with  $\text{CuFeS}_2 + \text{H}_2\text{O}_2$  was rough and wrinkled, or even ruptured. The cell structure of ESBL and PA was seriously damaged, and large areas of cavities could be clearly observed, while MRSA was characterized by severe bacterial shrinkage and a rough cell surface. In Figures S9 and S11, we added the SEM image of bacteria after the  $\text{CuFeS}_2 + \text{H}_2\text{O}_2 + \text{NIR}$  and  $\text{CuFeS}_2 + \text{H}_2\text{O}_2$ . The above results proved that both the  $\text{Cu}^{2+}$  release and ROS storm caused by  $\text{CuFeS}_2$  NPs peroxidase could cause severe damage to the cell structure, or even rupture, resulting in the death of bacteria. In addition, many particles were found to be attached to the surface of bacteria, which may be caused by the aggregation of the  $\text{CuFeS}_2$  NPs on the surface of cells. Meanwhile, the interaction between the  $\text{CuFeS}_2$  NPs and bacteria is conducive to the maximum killing of bacteria. In addition, the  $\text{CuFeS}_2$  NPs and GSH were co-incubated at 37 °C in phosphate buffer (pH 7.4, 0.1 M), and DTNB was used at the characteristic peak of GSH at 412 nm. The results showed that, with the increase of co-incubation time (0, 1, 3, 6 h), the UV absorption peak at 412 nm gradually weakened (Figure S6); when incubated for 6 h, the peak value was close to that of the PBS control group, which proved that  $\text{CuFeS}_2$  NPs could consume GSH under physiological conditions, and this GSH consumption ability might be attributed to the presence of Fe(III) in  $\text{CuFeS}_2$  NPs [32]. In the bacteriostatic process, the decrease in GSH level directly leads to the decrease of the bacteria's antioxidant level, which is conducive to the production of ROS catalyzed by peroxidase, thus producing a stronger antibacterial ability.

### 3.5. $\text{CuFeS}_2$ NPs for the Treatment of Wound Infection in Rats

Through a series of characterization, it has been proven that  $\text{CuFeS}_2$  NPs have excellent antibacterial ability. In order to evaluate the therapeutic ability of  $\text{CuFeS}_2$  NPs in the process of promoting wound healing, we established the bacteria-infected wound healing model with an MRSA-infected rat back wound. A total of eight groups (three rats per group) were set up. Under the condition with or without the irradiation of NIR, the wounds of rats were treated with PBS,  $\text{H}_2\text{O}_2$ ,  $\text{CuFeS}_2$ , and  $\text{CuFeS}_2 + \text{H}_2\text{O}_2$ , respectively. Due to the PPT/CDT synergistic antibacterial performance and GSH consumption ability under the physiological conditions,  $\text{CuFeS}_2$  could produce more ROS to inhibit bacteria and promote wound healing. In Figure 6a, the wound healing of rats at different time points (1, 3, 5, and 7 days) was compared. As expected, the  $\text{CuFeS}_2 + \text{H}_2\text{O}_2 + \text{NIR}$  (NIR 5 min,  $1.0 \text{ W cm}^{-2}$ , 808 nm)-treated rats had the best wound healing in all the control and experimental groups. In addition, the wound area memory of rats after 7 days of treatment was statistically analyzed, and the treatment effect was quantified based on the wound size on day 1 (Figure 6b). After  $\text{CuFeS}_2 + \text{H}_2\text{O}_2 + \text{NIR}$  treatment, the wound healed faster, and the wound area was the smallest. This proves that the PPT/CDT synergistic antibacterial system based on  $\text{CuFeS}_2$  has great application potential in practical antibacterial applications. At the same time, on the 7th day, the wound tissues of the rats with different treatments were taken, and the wound healing was analyzed via the H&E staining of tissue sections. In Figure 6c, no significant inflammation was found in the  $\text{CuFeS}_2 + \text{H}_2\text{O}_2 + \text{NIR}$ -treated wound tissue, indicating the good antibacterial and anti-wound infection ability of the system. In addition, compared to the control group, the new epithelial tissues in the  $\text{CuFeS}_2 + \text{H}_2\text{O}_2 + \text{NIR}$  group were thicker, and the inflammatory cells were significantly reduced, proving that the

PPT/CDT synergistic antibacterial system of  $\text{CuFeS}_2$  effectively inhibited wound infection and promoted the growth of new tissues.

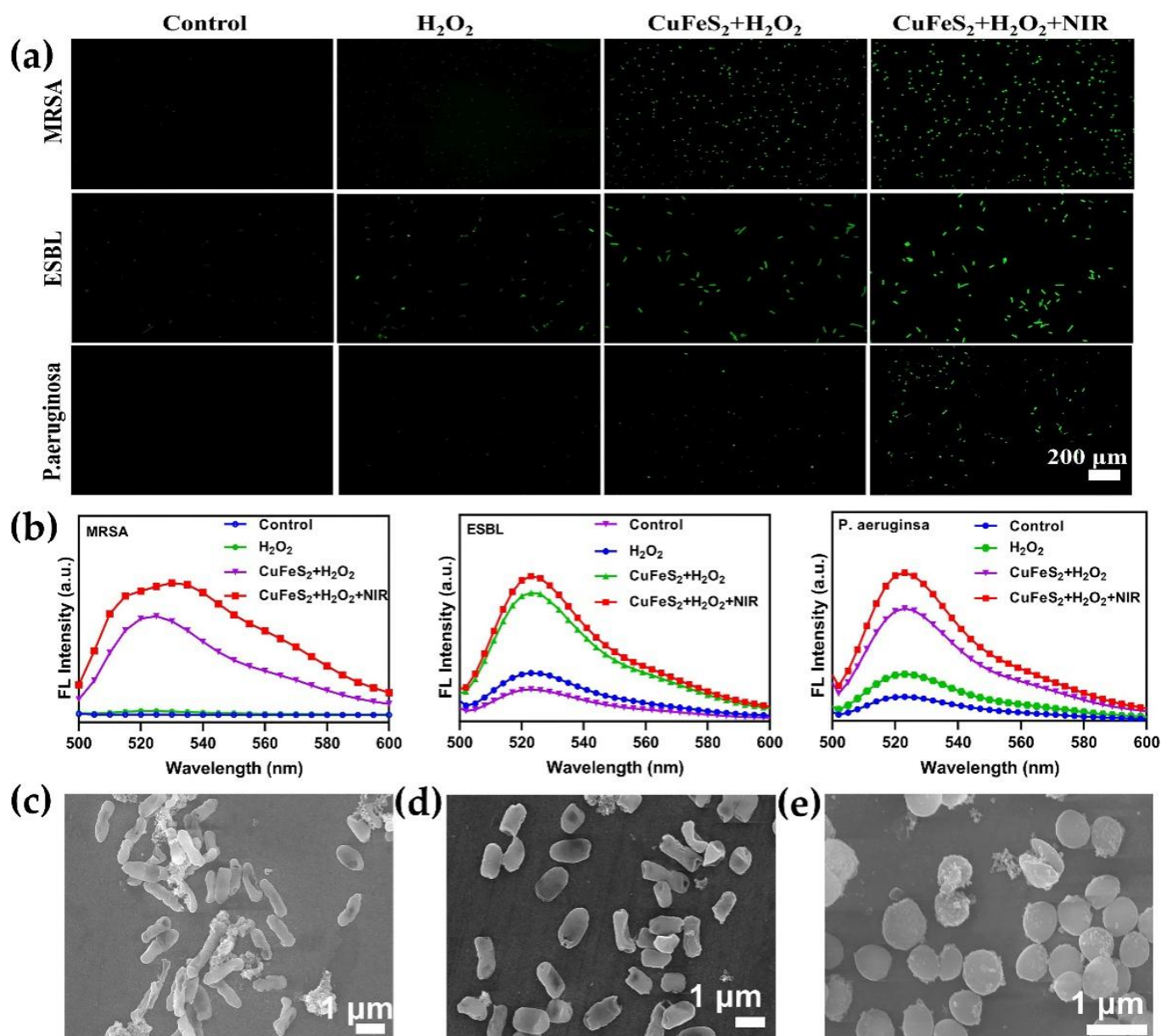


**Figure 5.** (a) After different treatments of PBS,  $\text{H}_2\text{O}_2$ ,  $\text{CuFeS}_2$ ,  $\text{CuFeS}_2 + \text{H}_2\text{O}_2$ , and  $\text{CuFeS}_2 + \text{H}_2\text{O}_2 + \text{NIR}$ , the ROS in MRSA, ESBL, and PA were labeled with fluorescent probes; (b) the corresponding fluorescence spectrum. Bar scale: 200  $\mu\text{m}$ . The SEM images of (c) PA, (d) ESBL, and (e) MRSA treated with  $\text{CuFeS}_2 + \text{H}_2\text{O}_2$ .

### 3.6. Biocompatibility of $\text{CuFeS}_2$ NPs

In vitro and in vivo antibacterial experiments have certified that the  $\text{CuFeS}_2$  NPs-based PTT/CDT antibacterial system has excellent antibacterial properties and can make infected wounds heal more easily. Therefore, it is indispensable to value the biosafety of  $\text{CuFeS}_2$  NPs. We used rat red blood cells as experimental materials to study the hemolysis characteristics of  $\text{CuFeS}_2$  NPs; no significant hemolysis was discovered, even in the presence of high concentration of  $\text{CuFeS}_2$  NPs ( $100 \mu\text{g mL}^{-1}$ ), and the hemolysis rate of  $\text{CuFeS}_2$  NPs was calculated to be about 1.4%, indicating that  $\text{CuFeS}_2$  NPS had good blood compatibility (Figure S7a). Figure S7b results showed that the L929 cells survival rate kept at about 100%,

even while the  $\text{CuFeS}_2$  NPS concentration reached  $32 \mu\text{g mL}^{-1}$ , which proved that  $\text{CuFeS}_2$  NPs had almost no toxicity to normal cells and good biocompatibility.

In addition, blood biochemical markers were measured by intravenous injection of  $\text{CuFeS}_2$  NPs into healthy rats (Figure 7a), and the results showed that blood indexes were normal, compared to the control group treated with PBS. As shown in Figure 7b, a histological analysis of the internal organs (kidney, spleen, liver, lung, and heart) of the rats showed no significant damage or inflammation. In conclusion, the prepared  $\text{CuFeS}_2$  NPs have good biocompatibility and are a potential antibacterial material.

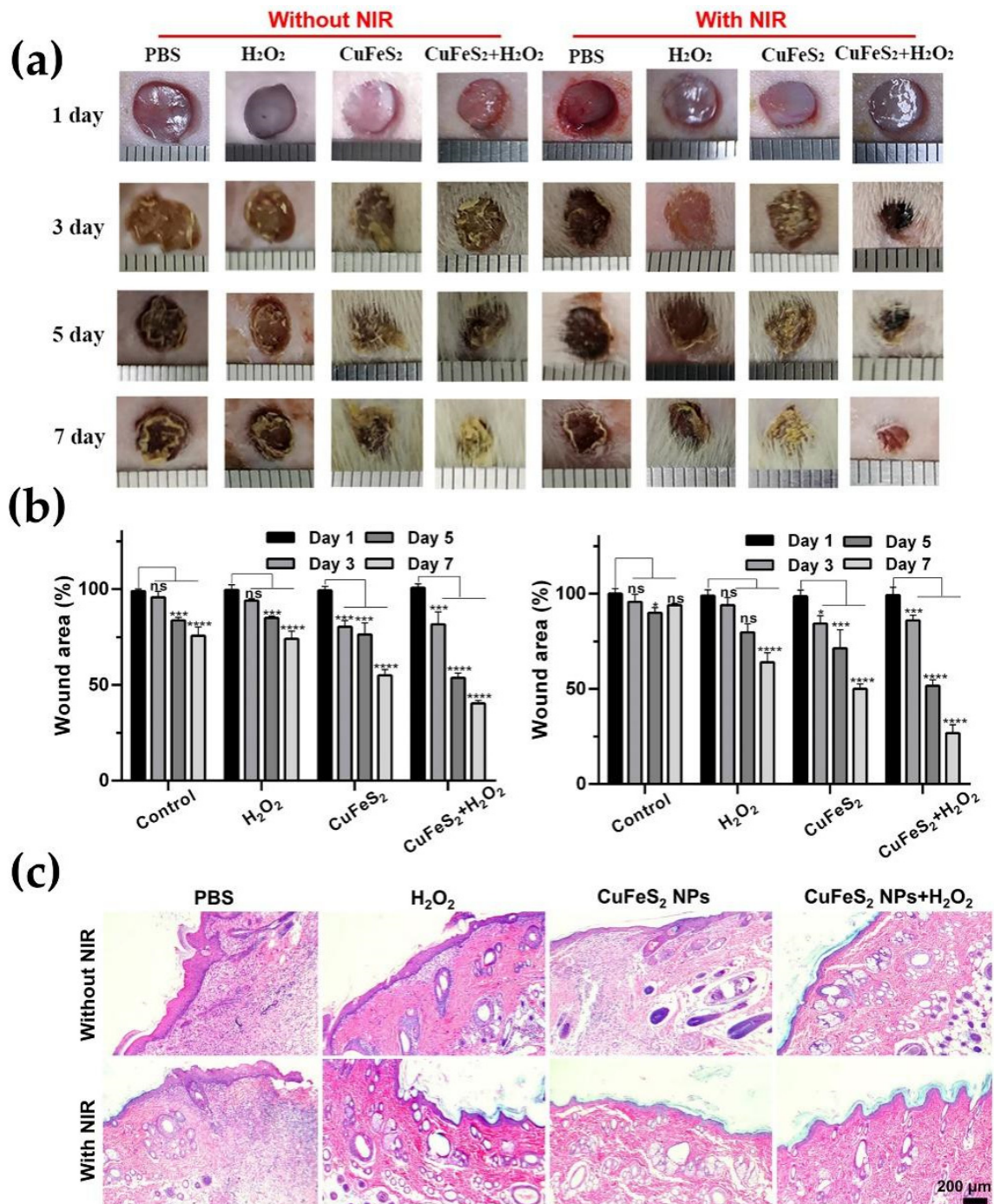


**Figure 6.** (a) Wound healing of rats at different times (day 1, 3, 5, and 7) after different treatments; (b) the corresponding wound area statistics ( $n = 3$ ). (c) Histological analysis of wound tissue after different treatments. Bar scale:  $200 \mu\text{m}$  (\*  $p < 0.05$ , \*\*\*  $p < 0.001$ , \*\*\*\*  $p < 0.0001$ ).

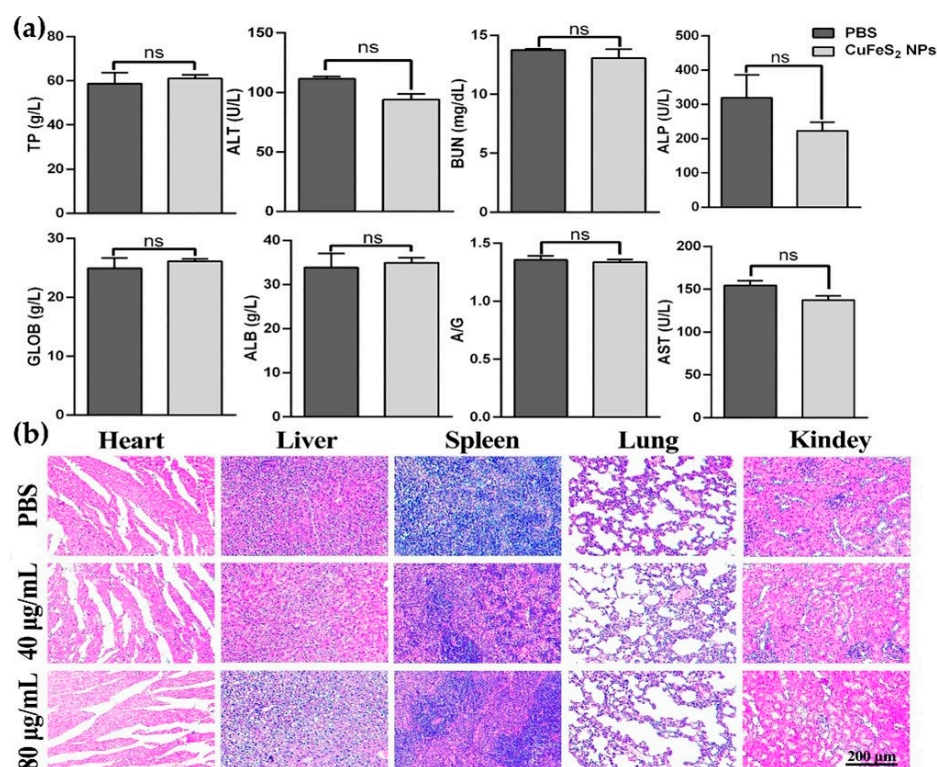


**Figure 7.** (a) Blood biochemical markers of rats after different treatments (PBS, 80  $\mu\text{g mL}^{-1}$  CuFeS<sub>2</sub> NPs). The terms are following: alkaline phosphatase (ALP), alanine transaminase (ALT), albumin (ALB), globulin (GLOB), aspartate transaminase (AST), total protein (TP), urea nitrogen (UREA), and the ratio of albumin and globulin (A/G). Error bars represented the standard deviation ( $n = 3$ ). (b) After different concentrations (40, 80  $\mu\text{g mL}^{-1}$ ) of CuFeS<sub>2</sub> NPs and PBS treatment, histological sections of internal organs of rats.

#### 4. Conclusions

In this work, CuFeS<sub>2</sub> NPs with small and uniform particle sizes were prepared at room temperature. The CuFeS<sub>2</sub> NPs have high peroxidase catalytic activity, excellent photothermal conversion ability, and good biocompatibility. Based on these excellent characteristics, the PTT/CDT synergistic antibacterial system of CuFeS<sub>2</sub> NPs was constructed, and the experimental results showed that the antibacterial system has high-efficiency and broad-spectrum antibacterial ability. Under NIR illumination, it can decompose a low concentration of H<sub>2</sub>O<sub>2</sub> into hydroxyl radicals under the catalysis of the internal peroxidase-like activity, thus achieving the purpose of a multimodal antibacterial, through the combination of near-distance ROS-mediated CDT and PTT. In addition, CuFeS<sub>2</sub> NPs can consume the GSH in bacteria and destroy the antioxidant balance of cells, which is more conducive to the generation of oxidative damage. Finally, the bacteriostatic rate of CuFeS<sub>2</sub> NPs (2.0  $\mu\text{g mL}^{-1}$ ) and H<sub>2</sub>O<sub>2</sub> (100  $\mu\text{M}$ ) was more than 99%, which assured the role of copper in the antibacterial effect, while reducing the agent amount significantly. In addition, in the treatment of MRSA wound infection in rats, the combined antibacterial system effectively inhibited the wound infection and promoted wound healing. More importantly, no obvious damage was observed to the internal organs of rats, which fully proved the safety of the antibacterial system. Therefore, this work proposes a safe and efficient antibacterial system, which brings new possibilities for fighting pathogenic bacteria and bacterial resistance and will greatly promote the further application of nanozymes in the treatment of bacterial infections and other diseases.

**Supplementary Materials:** The following are available online at <https://www.mdpi.com/article/10.3390/nano12142469/s1>. Figure S1: Diameter distribution of CuFeS<sub>2</sub> NPs. Figure S2: Temperature cycling test of CuFeS<sub>2</sub> NPs. Figure S3:  $\Delta$ PL intensity showed the catalytic activity of CuFeS<sub>2</sub>. Figure S4: Fluorescence intensity was measured by TA method. Figure S5: Fluorescence images of live/dead bacteria under different processing conditions. Bar scale: 20  $\mu$ m. Figure S6: Evaluation of GSH consumption capacity of CuFeS<sub>2</sub> NPs at different times. Figure S7: Cytotoxicity experiment of the CuFeS<sub>2</sub>. Figure S8: Visible–NIR absorption of CuFeS<sub>2</sub>. Figure S9: The SEM images of PA, ESBL, MRSA treated with CuFeS<sub>2</sub>+NIR+H<sub>2</sub>O<sub>2</sub>. Figure S10: Different-sized TEM image, HRTEM image. Figure S11: The SEM images of PA, ESBL and MRSA treated with CuFeS<sub>2</sub> +H<sub>2</sub>O<sub>2</sub>. Table S1: The Michaelis–Menten constants ( $K_m$ ) and maximum initial reaction rates ( $V_{max}$ ).

**Author Contributions:** Conceptualization, Z.L. (Zezhong Liu) and Z.L. (Zengxu Liu); methodology, Z.L. (Zengxu Liu); validation, Z.Z. and D.L.; formal analysis, Y.Z.; investigation, X.L.; resources, P.Z.; data curation, Y.X.; writing—original draft preparation, Z.L. (Zezhong Liu); writing—review and editing, X.D.; funding acquisition, Y.X. All authors have read and agreed to the published version of the manuscript.

**Funding:** This research was funded by the National Natural Science Foundation of China (Nos. 21874079 and 21575071), Natural Science Foundation for Outstanding Young Scientists of Shandong Province (ZR2018JL011), Key R&D Project of Shandong Province (GG201809230180), Qingdao Science and Technology Planning Project (17-6-3-15-gx), Qingdao Postdoctoral Applied Research Project (grant No. RZ2000003874), and Science and Technology Fund Planning Project of Shandong Colleges and Universities (J16LA13 and J18KA112).

**Institutional Review Board Statement:** In this experiment, the mouse fibroblast cell line L929 was obtained from the Institute of Biochemistry and Cell Biology of the Chinese Academy of Sciences.

**Informed Consent Statement:** Not applicable.

**Data Availability Statement:** The data presented in this study are available on request from the corresponding author.

**Conflicts of Interest:** The authors declare no conflict of interest.

## References

1. Wang, Q.; Jiang, J.; Gao, L. Catalytic antimicrobial therapy using nanozymes. *WIREs Nanomed. Nanobiotechnol.* **2021**, *14*, e1769. [[CrossRef](#)] [[PubMed](#)]
2. Li, T.; Sun, M.; Wu, S. State-of-the-art review of electrospun gelatin-based nanofiber dressings for wound healing applications. *Nanomaterials* **2022**, *12*, 784. [[CrossRef](#)] [[PubMed](#)]
3. Jones, K.E.; Patel, N.G.; Levy, M.A.; Storeygard, A.; Balk, D.; Gittleman, J.L.; Daszak, P. Global trends in emerging infectious diseases. *Nature* **2008**, *451*, 990–993. [[CrossRef](#)]
4. Yin, W.; Yu, J.; Lv, F.; Yan, L.; Zheng, L.R.; Gu, Z.; Zhao, Y. Functionalized Nano-MoS<sub>2</sub> with peroxidase catalytic and near-infrared photothermal activities for safe and synergetic wound antibacterial applications. *ACS Nano* **2016**, *10*, 11000–11011. [[CrossRef](#)] [[PubMed](#)]
5. Cao, F.; Zhang, L.; Wang, H.; You, Y.; Wang, Y.; Gao, N.; Ren, J.; Qu, X. Defect-rich adhesive nanozymes as efficient antibiotics for enhanced bacterial inhibition. *Angew. Chem.* **2019**, *58*, 16236–16242. [[CrossRef](#)]
6. Fang, Y.F.; Ding, X.T.; Xu, G.F.; Gong, S.D.; Niu, Y.S.; Yao, Z.Y.; Jin, Z.Y.; Wang, Y.; Xu, Y.H. Direct synthesis of bienzyme-like carbide-derived carbons via mild electrochemical oxidation of Ti<sub>3</sub>AlC<sub>2</sub> MAX. *Biomed. Env. Sci.* **2022**, *35*, 215–224.
7. Zhang, Y.F.; Li, D.X.; Xu, Y.H.; Niu, Y.S. Application of a cascaded nanozyme in infected wound recovery of diabetic mice. *ACS Biomater. Sci. Eng.* **2022**, *8*, 1522–1531. [[CrossRef](#)]
8. Raj, V.; Kim, Y.; Kim, Y.G.; Lee, J.H.; Lee, J. Chitosan-gum arabic embedded alizarin nanocarriers inhibit biofilm formation of multispecies microorganisms. *Carbohydr. Polym.* **2022**, *284*, 118959. [[CrossRef](#)]
9. Liu, B.; Wang, Y.; Chen, Y.; Guo, L.; Wei, G. Biomimetic two-dimensional nanozymes: Synthesis, hybridization, functional tailoring, and biosensor applications. *J. Mater. Chem. B* **2020**, *8*, 10065–10086. [[CrossRef](#)]
10. Wang, L.W.; Gao, F.N.; Wang, A.Z.; Chen, X.Y.; Li, H.; Zhang, X.; Zheng, H.; Ji, R.; Li, B.; Yu, X.; et al. Defect-rich adhesive molybdenum disulfide/rGO vertical heterostructures with enhanced nanozyme activity for smart bacterial killing application. *Adv. Mater.* **2020**, *32*, 2005423. [[CrossRef](#)]
11. Lin, Y.; Liu, X.; Liu, Z.; Xu, Y. Visible-light-driven photocatalysis-enhanced nanozyme of TiO<sub>2</sub> Nanotubes@MoS<sub>2</sub> nanoflowers for efficient wound healing infected with multidrug-resistant bacteria. *Small* **2021**, *17*, 210327. [[CrossRef](#)] [[PubMed](#)]
12. Lin, J.J.; Lin, W.C.; Li, S.D.; Lin, C.Y.; Hsu, S.H. Evaluation of the antibacterial activity and biocompatibility for silver nanoparticles immobilized on nano silicate platelets. *ACS Appl. Mater. Inter.* **2013**, *5*, 433–443. [[CrossRef](#)] [[PubMed](#)]

13. Yu, Z.; Sun, Q.; Pan, W.; Li, N.; Tang, B. A near-Infrared triggered nanophotosensitizer inducing domino effect on mitochondrial reactive oxygen species burst for cancer therapy. *ACS Nano* **2015**, *9*, 11064–11074. [[CrossRef](#)] [[PubMed](#)]
14. Gao, Q.; Zhang, X.; Yin, W.; Ma, D.; Xie, C.; Zheng, L.; Dong, X.; Mei, L.; Yu, J.; Wang, C.; et al. Functionalized MoS<sub>2</sub> nanovehicle with near-infrared laser-mediated nitric oxide release and photothermal activities for advanced bacteria-infected wound therapy. *Small* **2018**, *14*, 1802290. [[CrossRef](#)]
15. Aksoy, İ.; Küçükkeçeci, H.; Sevgi, F.; Metin, Ö.; Hatay Patir, I. Photothermal antibacterial and antibiofilm activity of black phosphorus/gold nanocomposites against pathogenic bacteria. *ACS Appl. Mater. Inter.* **2020**, *12*, 26822–26831. [[CrossRef](#)]
16. He, H.; Yang, Q.; Li, H.; Meng, S.; Xu, Z.; Chen, X.; Sun, Z.; Jiang, B.; Li, C. Hollow mesoporous MnO<sub>2</sub>-carbon nanodot-based nanoplatform for GSH depletion enhanced chemodynamic therapy, chemotherapy, and normal/cancer cell differentiation. *Mikrochim. Acta* **2021**, *188*, 141. [[CrossRef](#)]
17. Meng, X.; Zhang, X.; Lei, Y.; Cao, D.; Wang, Z. Biodegradable copper-metformin nanoscale coordination polymers for enhanced chemo/chemodynamic synergistic therapy by reducing oxygen consumption to promote H<sub>2</sub>O<sub>2</sub> accumulation. *J. Mater. Chem. B* **2021**, *9*, 1988–2000. [[CrossRef](#)]
18. Chen, Q.; Luo, Y.; Du, W.; Liu, Z.; Zhang, S.; Yang, J.; Yao, H.; Liu, T.; Ma, M.; Chen, H. Clearable theranostic platform with a pH-independent chemodynamic therapy enhancement strategy for synergetic photothermal tumor therapy. *ACS Appl. Mater. Inter.* **2019**, *11*, 18133–18144. [[CrossRef](#)]
19. Velásquez, P.; Leinen, D.; Pascual, J.; Ramos-Barrado, J.R.; Grez, P.; Gómez, H.; Schrebler, R.; del Río, R.; Córdova, R. A chemical, morphological, and electrochemical (XPS, SEM/EDX, CV, and EIS) analysis of electrochemically modified electrode surfaces of natural chalcopyrite (CuFeS<sub>2</sub>) and pyrite (FeS<sub>2</sub>) in alkaline solutions. *J. Phys. Chem. B* **2005**, *109*, 4977–4988. [[CrossRef](#)]
20. Yang, A.; Huangfu, X.; Liu, L.; Luo, W.; Zhao, W.; Yin, J. Electrochemiluminescence immunosensor based on signal probe CuFeS<sub>2</sub> quantum dots for ultrasensitive detection of cyclin D1. *Electroanal. Chem.* **2020**, *871*, 114269. [[CrossRef](#)]
21. Ghahremaninezhad, A.; Dixon, D.G.; Asselin, E. Electrochemical and XPS analysis of chalcopyrite (CuFeS<sub>2</sub>) dissolution in sulfuric acid solution. *Electrochim. Acta* **2013**, *87*, 97–112. [[CrossRef](#)]
22. Sahoo, S.; Pazhamalai, P.; Mariappan, V.K.; Veerasubramani, G.K.; Kim, N.-J.; Kim, S.-J. Hydrothermally synthesized chalcopyrite platelets as an electrode material for symmetric supercapacitors. *Inorg. Chem. Front.* **2020**, *7*, 1492–1502. [[CrossRef](#)]
23. Xu, X.; Tang, D.; Cai, J.; Xi, B.; Zhang, Y.; Pi, L.; Mao, X. Heterogeneous activation of peroxymonocarbonate by chalcopyrite (CuFeS<sub>2</sub>) for efficient degradation of 2,4-dichlorophenol in simulated groundwater. *Appl. Catal. B Environ.* **2019**, *251*, 273–282. [[CrossRef](#)]
24. Zhou, J.; Jiang, F.; Li, S.; Xu, Z.; Sun, W.; Ji, X.; Yang, Y. CuFeS<sub>2</sub> as an anode material with an enhanced electrochemical performance for lithium-ion batteries fabricated from natural ore chalcopyrite. *J. Solid State Electr.* **2019**, *23*, 1991–2000. [[CrossRef](#)]
25. Deen, K.M.; Asselin, E. On the use of a naturally-sourced CuFeS<sub>2</sub> mineral concentrate for energy storage. *Electrochim. Acta* **2019**, *297*, 1079–1093. [[CrossRef](#)]
26. Da Silveira Salla, J.; Dotto, G.L.; Hotza, D.; Landers, R.; da Boit Martinello, K.; Foletto, E.L. Enhanced catalytic performance of CuFeS<sub>2</sub> chalcogenide prepared by microwave-assisted route for photo-fenton oxidation of emerging pollutant in water. *J. Environ. Chem. Eng.* **2020**, *8*, 104077. [[CrossRef](#)]
27. Zhang, Y.; Li, D.; Tan, J.; Chang, Z.; Liu, X.; Ma, W.; Xu, Y. Near-infrared regulated nanozymatic/photothermal/photodynamic triple-therapy for combating multidrug-resistant bacterial infections via oxygen-vacancy molybdenum trioxide nanodots. *Small* **2021**, *17*, 2005739. [[CrossRef](#)]
28. Zeng, J.; Goldfeld, D.; Xia, Y. A plasmon-assisted optofluidic (PAOF) system for measuring the photothermal conversion efficiencies of gold nanostructures and controlling an electrical switch. *Angew. Chem.* **2013**, *52*, 4169–4173. [[CrossRef](#)]
29. Gao, L.; Zhuang, J.; Nie, L.; Zhang, J.; Zhang, Y.; Gu, N.; Wang, T.; Feng, J.; Yang, D.; Perrett, S.; et al. Intrinsic peroxidase-like activity of ferromagnetic nanoparticles. *Nat. Nanotechnol.* **2007**, *2*, 577–583. [[CrossRef](#)]
30. Song, C.; Ding, W.; Zhao, W.; Liu, H.; Wang, J.; Yao, Y.; Yao, C. High peroxidase-like activity realized by facile synthesis of FeS<sub>2</sub> nanoparticles for sensitive colorimetric detection of H<sub>2</sub>O<sub>2</sub> and glutathione. *Biosens. Bioelectron.* **2020**, *151*, 111983. [[CrossRef](#)]
31. Manyasree, D.; Kiran Mayi, P.; Ravikumar, R. CuO nanoparticles: Synthesis, characterization and their bactericidal efficacy. *Int. J. App. Pharm.* **2017**, *9*, 71–74.
32. Li, J.; Hu, Z.E.; We, Y.J.; Liu, Y.H.; Wang, N.; Yu, X.Q. Multifunctional carbon quantum dots as a theranostic nanomedicine for fluorescence imaging-guided glutathione depletion to improve chemodynamic therapy. *J. Colloid Interf. Sci.* **2022**, *606*, 1219–1228. [[CrossRef](#)] [[PubMed](#)]